Tian, B., Merino, M. y Ahedo, E. (2018). Two-dimensional plasma-wave interaction in an helicon plasma thruster with magnetic nozzle. *Plasma Sources Science and Technology*, 27(11).

DOI: https://doi.org/10.1088/1361-6595/aaec32

Two-dimensional plasma-wave interaction in an helicon plasma thruster with magnetic nozzle

Bin Tian,[1, a)] Mario Merino,[1] and Eduardo Ahedo[1]

Equipo de Propulsión Espacial y Plasmas (EP2), Universidad Carlos III de Madrid, 28911 Leganés, Spain

An axisymmetric, finite difference frequency domain model is used to study the wave propagation and power absorption in a helicon plasma thruster operating inside a laboratory vacuum chamber. The magnetic field is not purely axial and the plasma beam is cylindrical in the source and divergent in the magnetic nozzle. The influence of the magnetic field strength, plasma density, electron collision frequency and geometry on the wavefields and the power absorption maps is investigated, showing different power deposition patterns. The electromagnetic radiation is not confined to the source region but propagates into the nozzle divergent region, and indeed the power absorption there is not negligible. For the impedance at the antenna, the reactance is rather constant but the resistance is very dependent on operation parameters; optimal parameter values maximizing the resistance are found.

PACS numbers: 52.75.Di

Keywords: electric space propulsion, helicon plasma thruster, plasma-wave interaction, helicon waves, wave heating

[a)]Electronic mail: ep2@uc3m.es; http://ep2.uc3m.es

I. INTRODUCTION

The Helicon Plasma Thruster (HPT) is an innovative space propulsion technology which has been under research and development during the last decade[1–7]. Following Ahedo[8], an HPT has two stages: a helicon plasma source[9,10] where the plasma is generated and heated, and a magnetic nozzle[11,12] where the plasma beam is accelerated supersonically. The helicon source is a cylindrical chamber with a neutral gas injector and a radiofrequency (RF) emitter (or antenna) wrapped around it, which emits waves into the plasma. A longitudinal magnetic field, created by coils or magnets around the source, is an essential element of the device for three reasons: (i) to enable the propagation of helicon waves inside the plasma column, (ii) to confine magnetically the plasma off the chamber walls, and (iii) to create the divergent magnetic nozzle. Thrust is achieved both mechanically, by the plasma pressure acting axially inside the source, and magnetically, by the reaction force created by the azimuthal plasma currents on the thruster coils or magnets[8,13]. Maximizing the magnetic contribution to thrust is desirable to improve the device efficiency. Among the potential advantages as a competitive space propulsion system, the HPT would be a long-life, alternative-propellant-friendly, simple-to-control device, since it has no internal electrodes or grids, and the chamber walls are magnetically protected. Good throttleability and extensive power-scaling of the HPT are claimed too. However, HPT technology is still in its infancy, with several aspects of its operation currently not well understood, and with prototypes that display a low thrust efficiency (typically about 10% or lower[14,15]).

From an energetic viewpoint, the HPT is an electrothermal device, where RF energy is deposited (mostly) onto electrons through plasma-wave interaction processes. Part of this electron internal energy is consumed in ionizing the neutral gas and the rest is transferred to ions as direct kinetic energy, via the ambipolar electric field created by the plasma itself. Ahedo and Navarro[16] developed an ideal two-dimensional (2D) model of the axisymmetric plasma discharge in an HPT and quantified the thruster performance and partial efficiencies, and Ahedo and Merino[11] developed a 2D model of the plasma expansion in the magnetic nozzle region. It was concluded that an efficient thruster must not only have good propellant utilization and plasma confinement, but must also achieve a large electron temperature, as the performances of the device (thrust, specific impulse) scale with it. It is also essential that the RF power be deposited in the plasma inside the source, to maximize its utilization

in the expansion that takes place in the magnetic nozzle region. The experimental evidence from HPT testing in laboratory vacuum chambers is that the electron temperature is too low generally (say, below 10 eV). Further development and testing of HPT prototypes must demonstrate that higher temperatures are achievable with modified designs or regimes of operation. Meanwhile, theory and simulation should help unveil how to achieve it and understand the power deposition pattern in the plasma by the antenna. This paper attempts to contribute to advance in this problem from that second way. A parallel field of research is the design of an efficient RF generator and the associated matching circuit. Beyond the intrinsic electrical efficiency of the generator there is the one related to a good matching with the antenna/plasma, which depends on the impedance seen by the antenna. Having a stable, relatively large resistance and small reactance across all operating points is desirable to simplify its design. An analysis of the influence of the design and operational parameters on antenna impedance is a main contribution of this work.

The Ahedo-Navarro axisymmetric fluid model assumes a known electron temperature, which is then correlated with the absorbed energy by the plasma, and thus avoids totally the plasma-wave interaction process. In this paper, an axisymmetric electromagnetic wave model capable of determining the 2D wave fields and the map of absorbed energy in the non-cylindrical plasma is developed. This will allow that ultimately the 'RF-wave absorption' and the 'quasi-stationary plasma transport' models be coupled and a consistent solution of the whole problem be obtained. The plasma-wave model is used here to analyze the dependency of the wave fields, absorbed power, and the antenna impedance on the operational parameters of the HPT, including the applied magnetic field, the plasma density, and the overall electron collisionality. These results also allow assessing the fraction of radiated power that is not absorbed directly inside the plasma source, which may lead to a decrease of performance of the device. The target configuration of the present study is a HPT operating inside a laboratory vacuum chamber, as this is currently the most relevant one in the current state of research of this technology.

A similar axisymmetric cold plasma-wave interaction model to the one used in this work has been developed previously in the literature independently by Mouzouris and Scharer[17], Carter et al.[18], and Chen et al.[19]. However, these works applied their axisymmetric model only to a cylindrical plasma and an axial magnetic field. On the other hand Kinder et al.[20] employ a 2D plasma-wave model, based on a simplified conductivity tensor that is

valid for the azimuthal mode $m = 0$, to obtain the wave fields and then study the electron distribution function with Monte Carlo simulations in an inductively-coupled plasma source for material processing applications. The contribution of this paper is the extension of the full 2D cold plasma-wave model to topologies with non-axial orientations of the applied magnetic field vector $\boldsymbol{B}_a$, and the study of the influence of a partially-divergent plasma beam in the magnetic nozzle region outside of the plasma source (which is the case of interest for HPT simulations) on wave propagation and absorption.

The rest of the paper is organized as follows. The general 2D plasma-wave model is presented in Section II. That section also comments on the loss of advantages of the used Yee's staggered-grid scheme[19,21] due to (i) a non-diagonal dielectric plasma tensor, and (ii) the misalignment of the magnetic field and the dielectric plasma tensor principal directions with the axial-radial Cartesian grid. Section III analyzes the nominal simulation case and the preeminence of the $m = 1$ mode in plasma-wave interaction. Section IV carries out an investigation of the plasma-wave response in terms of the operation parameters and discusses the influence of the divergence of the plasma plume. Section V presents the conclusions. A preliminary version of this work was presented in a conference paper[22].

II. 2D PLASMA-WAVE MODEL

The meridian plane of a typical HPT operating in a cylindrical laboratory vacuum chamber of length L and radius r_w is sketched in Fig. 1. The helicon source itself is a dielectric tube of radius r_s, length L_s, and negligible thickness, separated a distance L_v from the rear wall of the vacuum chamber. The contribution of the thin dielectric tube to the wave propagation problem is known to be small[23], and is not included in the present model. A magnetic circuit made of coils and/or permanent magnets, not shown in the figure, generates an applied magnetic field $\boldsymbol{B}_a(z,r)$ whose local angle with the thruster axis is $\alpha(z,r)$:

$$\boldsymbol{B}_a(z,r) = B_a(z,r)[\mathbf{1}_z \cos\alpha(z,r) + \mathbf{1}_r \sin\alpha(z,r)]. \tag{1}$$

The plasma is generated in the cylindrical source and then emitted as a divergent jet channeled by a magnetic streamsurface. The plasma jet radius $r_p = r_p(z)$ is constant inside the source, where $r_p(z) = r_s$, and increases outside with the expanding magnetic field until it reaches the downstream vacuum chamber wall. A radiating antenna is wrapped around the

source which has a median radius r_a, thickness d_t, and length L_a, and emits electromagnetic power at angular frequency ω, typically in the range $1 - 100$ MHz[24].

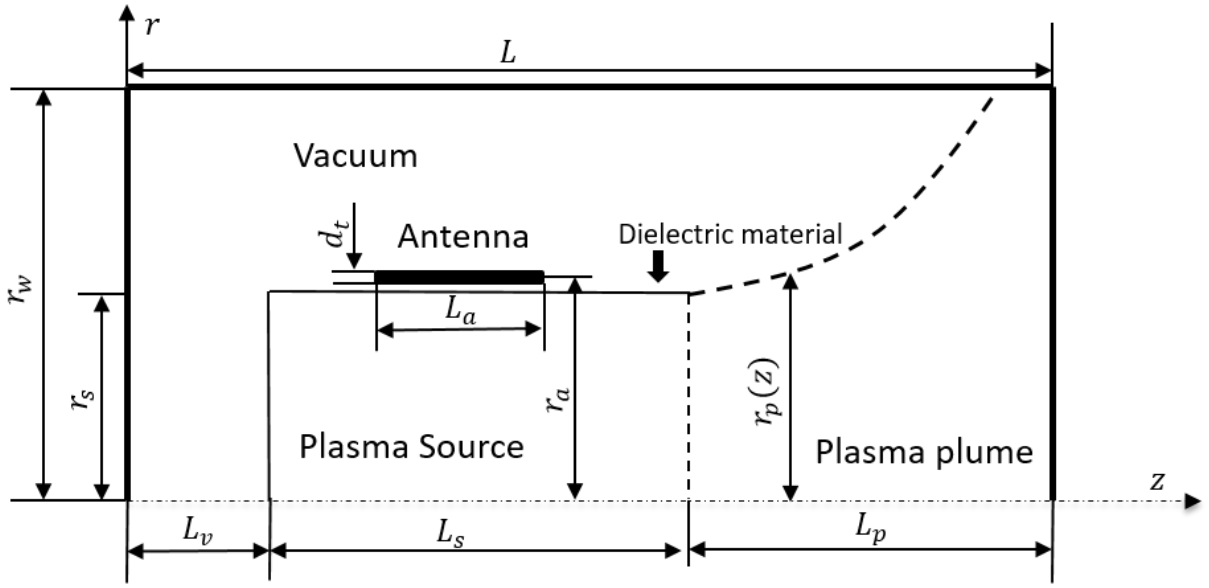

FIG. 1. Sketch of the geometry of the helicon plasma thruster used in the 2D plasma wave model.

The electromagnetic radiation propagates from the antenna into the surrounding vacuum as dictated by Maxwell equations. The plasma inside the helicon source and in the magnetic nozzle affects the RF power propagation, and absorbs part of it as it traverses the plasma domain. While kinetic effects, such as Landau damping, can play a role under certain operation regimes, the dominant absorption mechanism at large plasma densities (expected in the operation of an efficient HPT) is collisional absorption[25]. Furthermore, when the amplitude of the RF fields is small compared to the DC electromagnetic fields[26] (i.e. the applied magnetic field and the ambipolar electric field), the plasma RF response can be linearized about its instantaneous DC state. Under these assumptions, the axisymmetric plasma-wave interaction model reduces to solving the Maxwell equations with a cold plasma dielectric tensor. The Fourier transform can be applied to time and the azimuthal direction, thus obtaining independently the response to each wave frequency ω and azimuthal wave mode m.

Expressing the wavefield as the product of the complex magnitudes $(E_z, E_r, E_\theta, B_z, B_r, B_\theta)$ and the phasor $\exp(im\theta - i\omega t)$, Maxwell equations for each azimuthal m mode are written

as follows[19]:

$$\frac{im}{r}E_z - \frac{\partial}{\partial z}E_\theta - i\omega B_r = 0, \tag{2}$$

$$\frac{\partial}{\partial z}E_r - \frac{\partial}{\partial r}E_z - i\omega B_\theta = 0, \tag{3}$$

$$\frac{1}{r}\frac{\partial}{\partial r}\left(rE_\theta\right) - \frac{im}{r}E_r - i\omega B_z = 0, \tag{4}$$

$$\frac{im}{r}B_z - \frac{\partial}{\partial z}B_\theta + i\omega\mu_0 D_r = \mu_0 j_{ar}, \tag{5}$$

$$\frac{\partial}{\partial z}B_r - \frac{\partial}{\partial r}B_z + i\omega\mu_0 D_\theta = \mu_0 j_{a\theta}, \tag{6}$$

$$\frac{1}{r}\frac{\partial}{\partial r}\left(rB_\theta\right) - \frac{im}{r}B_r + i\omega\mu_0 D_z = \mu_0 j_{az}, \tag{7}$$

where the explicit indication of m and ω has been omitted for all variables, the vector source term $\boldsymbol{j}_a(z,r)$ is the Fourier-expanded applied antenna current density, and $\boldsymbol{D}$ is the electric displacement field, expressed as

$$\boldsymbol{D} = \varepsilon_0\boldsymbol{E} + \frac{i\boldsymbol{j}_p}{\omega} = \varepsilon_0\bar{\bar{\kappa}}(z,r)\cdot\boldsymbol{E}, \tag{8}$$

with $\boldsymbol{j}_p$ the complex magnitude of the plasma current density, ε_0 the permittivity in vacuum, and

$$\bar{\bar{\kappa}}(z,r) = \begin{bmatrix} \kappa_1\cos^2\alpha + \kappa_3\sin^2\alpha & i\kappa_2\cos\alpha & (\kappa_3-\kappa_1)\sin(2\alpha)/2 \\ -i\kappa_2\cos\alpha & \kappa_1 & i\kappa_2\sin\alpha \\ (\kappa_3-\kappa_1)\sin(2\alpha)/2 & -i\kappa_2\sin\alpha & \kappa_3\cos^2\alpha + \kappa_1\sin^2\alpha \end{bmatrix}$$

the normalized cold plasma dielectric tensor rotated an angle $\alpha(z,r)$. In this last expression, the κ_j $(j=1,2,3)$ parameters are[27]:

$$\kappa_1 = 1 - \sum_{k=i,e}\frac{\omega_{pk}^2\left(\omega+i\nu_k\right)}{\omega\left[\left(\omega+i\nu_k\right)^2-\omega_{ck}^2\right]}, \tag{9}$$

$$\kappa_2 = -\sum_{k=i,e}\frac{s_k\omega_{ck}\omega_{pk}^2}{\omega\left[\left(\omega+i\nu_k\right)^2-\omega_{ck}^2\right]}, \tag{10}$$

$$\kappa_3 = 1 - \sum_{k=i,e}\frac{\omega_{pk}^2}{\omega\left(\omega+i\nu_k\right)}, \tag{11}$$

where $k=i,e$ for ions and electrons; ω_{pk}, ω_{ck} and ν_k are the plasma, cyclotron, and collision frequency of species k; and $s_i=+1$, $s_e=-1$. The dielectric tensor depends on the applied magnetic field vector $\boldsymbol{B}_a(z,r)$, the DC plasma density $n(z,r)$, and the electron collision

frequency $\nu_e(z,r)$. Outside of the plasma domain, i.e. in vacuum, $\bar{\bar{\kappa}}$ reduces to the identity tensor.

As in Ref. 19, the metal walls of the laboratory vacuum chamber are modeled as a perfect conductor for what regards electromagnetic wave propagation.

$$\begin{aligned} E_r = E_\theta = B_z = 0, \quad &\text{at } (0,r)\,,\ (L,r)\,, \\ E_z = E_\theta = B_r = 0, \quad &\text{at } (z,r_w)\,. \end{aligned} \tag{12}$$

Lastly, at the axis of symmetry $(z,0)$, the wave fields must be continuous and bounded. Consequently, each m mode must satisfy the following regularity conditions as $r \to 0$:

$$E_z, B_z \sim r^{|m|}, \tag{13}$$

$$(E_r + iE_\theta), (B_r + iB_\theta) \sim r^{|m+1|}, \tag{14}$$

$$(E_r - iE_\theta), (B_r - iB_\theta) \sim r^{|m-1|}. \tag{15}$$

For instance, for $m = 1$, the condition $E_z, B_z, E_r + iE_\theta, B_r + iB_\theta = 0$ is set at the symmetry axis, but $E_r - iE_\theta$ and $B_r - iB_\theta$ are free quantities.

A. Numerical discretization

The finite different scheme by Yee[21] is applied on a uniform Cartesian grid in (z,r) to discretize Eq. (2)–(7) into a matrix problem, which is then solved numerically for $\boldsymbol{E}$ and $\boldsymbol{B}$ on the grid nodes with a direct serial solver.

The use of Yee's algorithm in an axisymmetric plasma cylinder was described by Chen et al.[19] in detail. It is noteworthy that the odd-even grid separation that allows the definition of the well-known staggered grids in Yee's scheme for electromagnetic wave propagation in vacuum is not present in the case of a magnetized plasma. This is due to the existence of off-diagonal terms in the dielectric plasma tensor[28], and brings up the need to have all three components of $\boldsymbol{E}$ at all nodes in order to compute the components of $\boldsymbol{D}$. In the present work, the staggered grids approach is nonetheless implemented, making use of linear interpolation to obtain those components of $\boldsymbol{E}$ that are otherwise unavailable in each grid[19,23].

The helicon wave branch of the collisionless plasma dispersion relation has a resonance cone on which the wave number k goes to infinite[27]. The axis of this cone is aligned with the direction of the applied magnetic field $\boldsymbol{B}_a$. The existence of a resonance cone introduces

fundamental difficulties for the numerical simulation in this regime, as a numerical cell size smaller than the smallest wavelength is required to avoid numerical dispersion and spurious solutions[29].

Additionally, when the direction of the applied magnetic field differs from the grid directions by a magnetic angle $\alpha(z,r)$, new numerical dispersion and spurious solution difficulties exist[30]. This consideration further restricts the maximum numerical cell size.

Simulating a plasma with negligible collisionality ($\nu_e \to 0$) is hard due to the unboundedly large physical k. Collisionality ν_e limits the maximum k of the dispersion relation near the resonant cone directions, facilitating numerical integration. In the present work, the numerical grid has been chosen with this constraint in mind for the different cases: Each of the four staggered regular Cartesian grid used has $N_z \times N_r = 4400 \times 1100$ nodes, which for the chamber geometry gives a cell size with $\Delta z = 3.4 \cdot 10^{-3}$ cm, $\Delta r = 1.8 \cdot 10^{-3}$ cm. Notice that the convergence of all simulation case in this paper with this scale of grid size has been verified. In addition, the convergence of the numerical scheme with decreasing mesh size and the verification of the present code against analytical 1D solutions was presented in Ref. 22 and 31.

B. Absorbed power density and antenna impedance

Once the wavefield has been computed, it is possible to obtain power-related quantities of interest. First, the (complex) power deposition density for mode m can be written as

$$w_p = \frac{\boldsymbol{j}_p^* \cdot \boldsymbol{E}}{2}, \tag{16}$$

and its real part, $\Re(w_p)(z,r)$, integrated over all modes m, is the power density deposited in the plasma, which is the main input for a plasma quasisteady transport model like the one of Ref. 16 used. The integral of $\Re(w_p)(z,r)$ over the plasma volume V_p gives the total absorbed power P_{abs} for that m mode. Moreover, energy conservation implies that P_{abs} equals the ideal antenna resistive power computed in the antenna volume V_a for mode m:

$$P_{abs} = \Re\left(\int_{V_p} w_p \mathrm{d}V_p\right) = -\Re\left(\int_{V_a} \frac{\boldsymbol{j}_a^* \cdot \boldsymbol{E}}{2} \mathrm{d}V_a\right). \tag{17}$$

The impedance Z felt by the antenna for mode m is defined as the ratio of the complex power over $|I_a|^2/2$, where I_a is the amplitude of the current through the antenna on mode

m:

$$Z \equiv R - iX = -\frac{1}{|I_a|^2} \int_{V_a} \boldsymbol{j}_a^* \cdot \boldsymbol{E} \mathrm{d}V_a. \tag{18}$$

The antenna impedance is a relevant figure for the design of the RF-circuit: a nearly-resistive impedance is desirable, and values close to 50 Ω can help matching with commercial components. Moreover, the RF-circuit must actively control for the changes in antenna impedance with plasma density and other parameters, so a nearly constant value of Z can help simplify the circuit design.

Finally, observe that since the azimuthal modes constitute an orthogonal basis, the *total* power absorption and the total antenna impedance can be computed as the sum of the contributions of each m mode.

III. NOMINAL SIMULATION CASE

This section presents and analyzes a nominal simulation case, which is later used as the reference case for the parametric investigation in Section IV. The parameters of the nominal configuration are summarized in Table I. These parameters are representative of current HPT laboratory prototypes[4,16]. A Nagoya III antenna is used, and its Fourier coefficients are given in Appendix A. Note that $j_{za}(z,r)$ and $j_{\theta a}(z,r)$ are only non-zero for odd m modes, for which $j_{za} = \text{const}$ and $j_{\theta a}(z,r) \sim 1/m$. To normalize the results, an antenna current of 1 A has been chosen.

In the plasma source, the plasma density profile is chosen to be Gaussian in the radial direction, $n(r)$, and the magnetic field is taken uniform and parallel to the thruster axis. In the plume region, the plasma density and magnetic field distributions are obtained self-consistently with the 2D magnetic nozzle model of Ref. 11, which integrates the fluid continuity and momentum equations for ions and electrons starting from the plasma profile at the magnetic throat. The normalized plasma density and magnetic field are shown in Fig. 2. The reference plasma density $n^\star$ and applied magnetic field $B_a^\star$ are chosen at the center of the helicon source. A constant electron collision frequency in the plasma domain $\nu_e = \nu_e^\star = \text{const}$ is used in order to study the dependency of the plasma response on collisionality independently of the rest of parameters and without relying on a particular collisional model (e.g. classical, anomalous collisions, etc).

After freezing all other parameters, the resulting model depends on three variables: the reference applied magnetic field strength, $B_a^\star$, the reference plasma density, $n^\star$, and the effective electron collision frequency $\nu_e^\star$. The values of these parameters in the nominal simulation are shown in the second part of Table I.

In the nominal parametric case, only the right-hand-polarized wave (whistler wave) propagates inside the plasma, while the left-hand-polarized wave is evanescent. The right-hand-polarized branch of the dispersion relation includes the helicon waves, at low angles from the direction of the local magnetic field vector, and the short-wavelength Trivelpiece-Gould waves at angles close to the resonance cone.

Parameter	**value**
Chamber length L	15 cm
Chamber radius r_w	2 cm
Plasma source radius r_s	1 cm
Plasma source length L_s	5 cm
Plasma plume length L_p	5 cm
Chamber-source separation distance L_v	5 cm
Antenna type	Nagoya III
Frequency of the RF emission f	13.56 MHz ($\omega = 85.2$ Mrad/s)
Antenna loop radius r_a	1.2 cm
Antenna length L_a	2.5 cm
Antenna central position z_a	7.5 cm
Antenna wire thickness d_t	0.2 cm
Total antenna current I_a	1 A
Reference applied magnetic field $B_a^\star$	150 G ($\omega_{ce}^\star/\omega = 31$)
Reference plasma density $n^\star$	3.8×10^{18} m^{-3} ($\omega_{pe}^\star/\omega = 1291$)
Reference electron collision frequency $\nu_e^\star$	8.52 MHz ($\nu_e^\star/\omega = 0.1$)

TABLE I. Parameters of nominal simulation case. The last three entries of the table are varied in the simulations of Section IV.

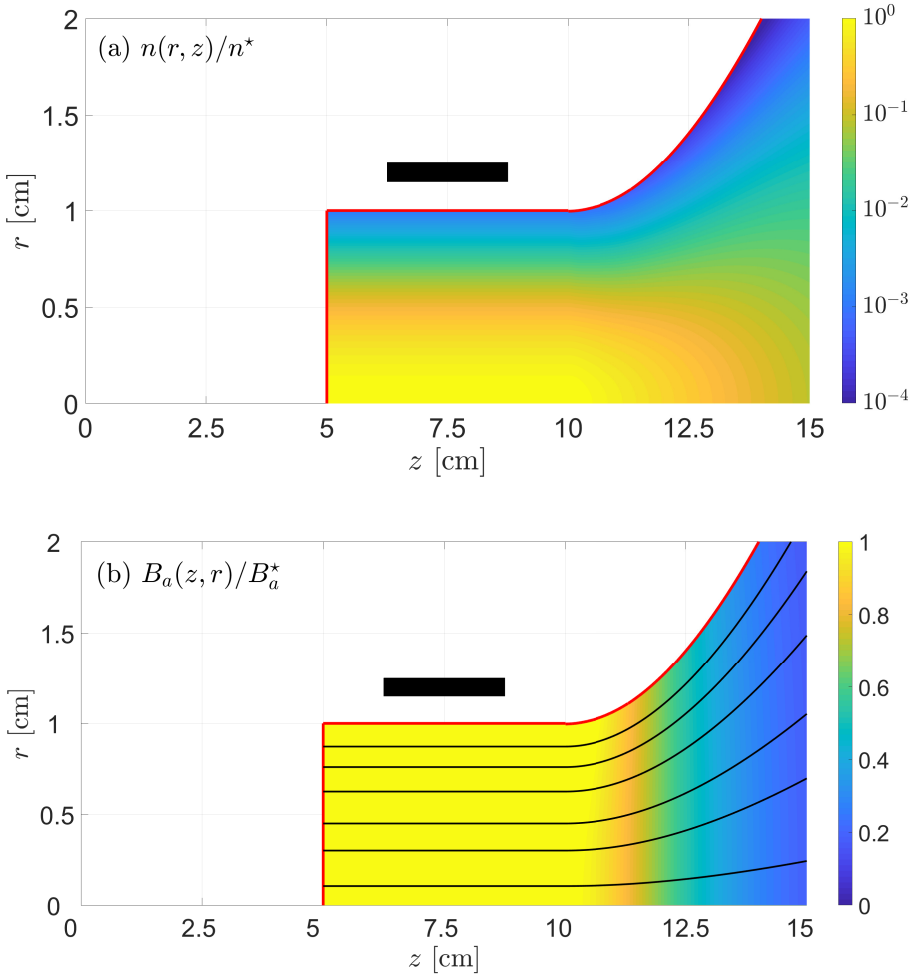

FIG. 2. Normalized profiles of plasma density $n(r,z)/n^\star$ and magnetic field $B_a(r,z)/B_a^\star$. The black rectangle indicates the location of the RF antenna; the red line delimits the extent of the plasma domain. Black lines in (b) are magnetic field lines.

A. Azimuthal modes

The contribution to antenna impedance of each m mode is shown in Fig. 3. The Nagoya III antenna excites only odd m modes. It is found that the resistance R and the reactance X decrease rapidly with increasing $|m|$, even though j_{za} is constant with m and $j_{\theta a}$ goes as $1/m$ (see Appendix A). It is evident, however, that (i) while X is essentially symmetric about $m = 0$, R is not, and that (ii) the $m = 1$ mode dominates over all other modes. This conclusion has been confirmed numerically and experimentally in helicon plasma sources[32–37], and is recovered here in the source-plume configuration. The other modes, while propagating, have

only a minor role in the plasma resistance and power absorption in the present model.

Figure 4 further illustrates this by showing the power absorption density $\Re(w_p)$ for modes $m = \pm 1, \pm 3$. The power absorption associated to all $m \neq 1$ modes is negligible compared to the $m = 1$ mode. It is also apparent that while power absorption for the $m \neq 1$ modes concentrates in the plasma source region, a notable part of the $m = 1$ mode power absorption takes place in the divergent plume region. The dominance of $m = 1$ is also true for all other non-nominal simulations carried out in this work. Hence, in the following, only the mode $m = 1$ will be considered for the wave field and absorbed power calculations.

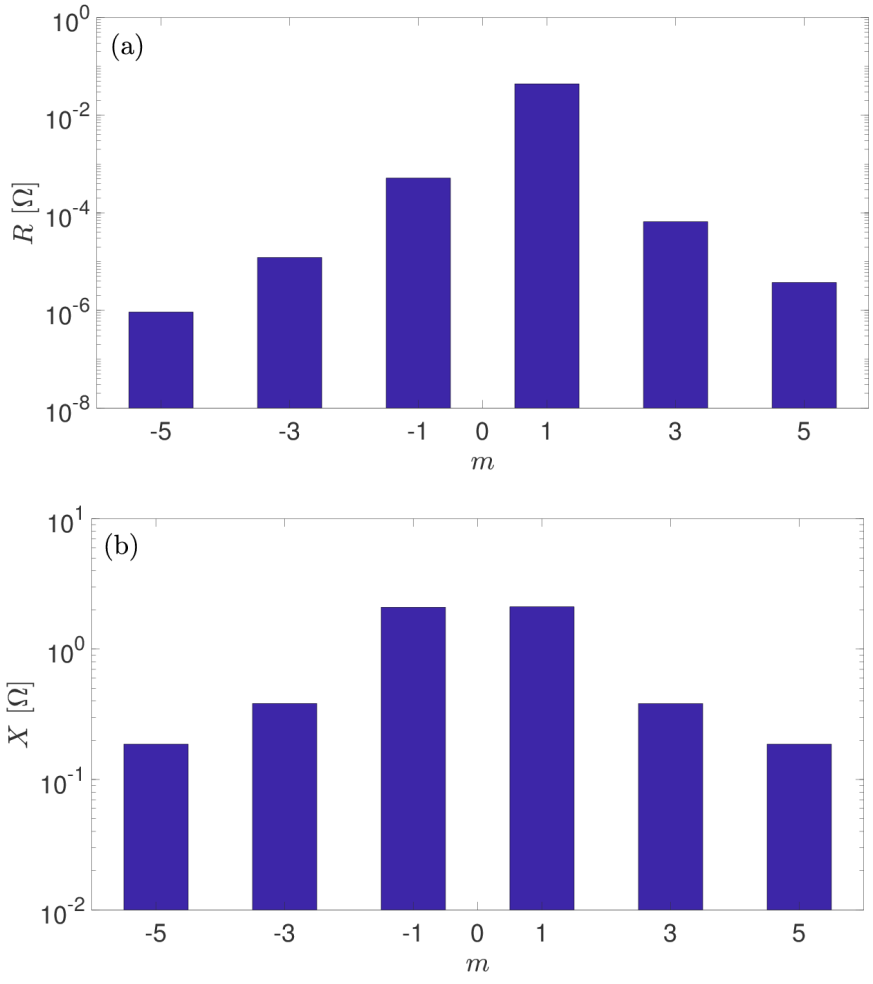

FIG. 3. Contribution to resistance and reactance at the antenna for each m mode in the nominal simulation case.

Fig. 5 shows the absolute value of the six wave field components for $m = 1$ in the nominal case. The standing wave structure in the closed vacuum chamber is evident from the presence

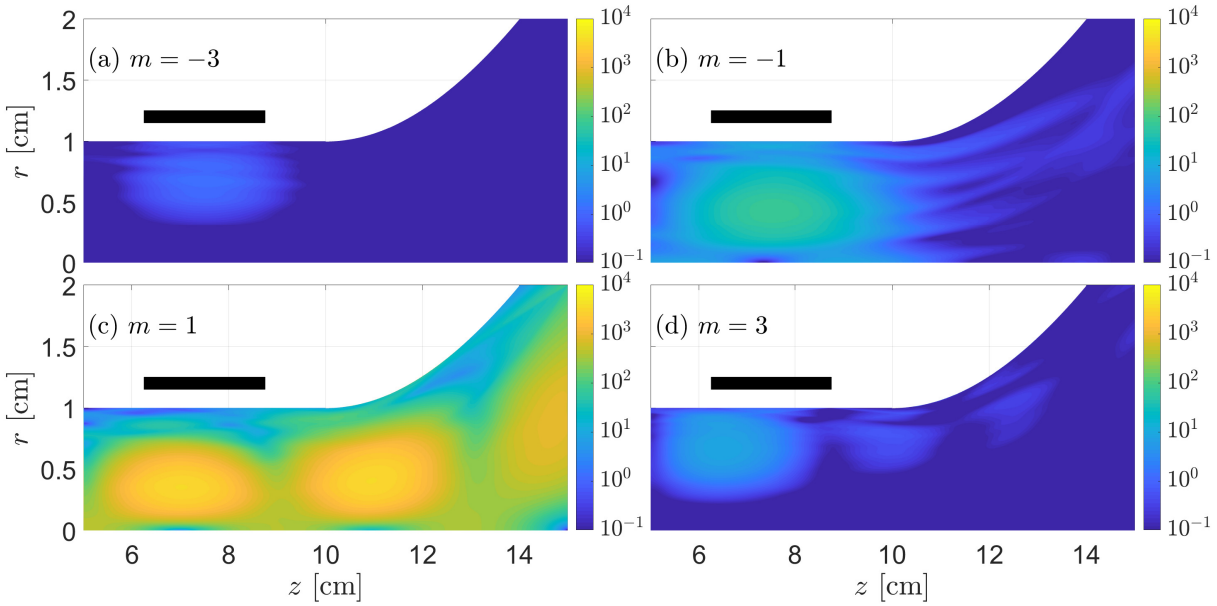

FIG. 4. 2D distribution of power absorption density $\Re(w_p)$ for different m modes in the nominal simulation case. All other parameters correspond to Table I.

of nodal surfaces in the solution. This can also be inferred from the existence of absorption peaks in Fig. 4, which are also observed in other simulations in the literature[19,20], and are consistent with the dispersion relation for non-uniform plasmas obtained by Breizman[38]. The presence of the divergent applied magnetic field in the plume region has a marked effect on the position, intensity and width of these hot regions, which are guided by the curved magnetic lines and roughly aligned along the middle-radius magnetic field tubes.

In the plasma domain, two distinct regions can be identified in the electric field plots. First, there is a region with short-wavelength waves near the plasma edge, where the intensity of the radial electric field, E_r, is large. These waves can be identified as the highly-oblique Trivelpiece-Gould (TG) waves. Second, a region with longer-wavelength, nearly-axial waves is identifiable in the bulk of the plasma. These waves correspond to the helicon mode, and in them both E_r and E_θ are excited. The axial structure of the wavefield is consistent with the power absorption peaks of Fig. 4. Comparison of Fig. 5 with 4 reveals that power absorption takes place mainly in the bulk region of the plasma. This suggests that the TG mode plays a minor role in power absorption in this particular simulation; this is not necessarily true for other parametric cases shown in this work, where absorption near the edge of the plasma is more relevant, as can be seen in Section IV.

Outside of the plasma domain, the wave electric field $\boldsymbol{E}$ is small, except near the antenna, but the wave magnetic field $\boldsymbol{B}$ is comparable inside and outside of it. Both the electric and magnetic wave fields are negligible in the back part of the chamber. For this reason, this part of the simulation is not included in the rest of figures in this article. On the other hand, the magnitude of $\boldsymbol{B}$ is comparable with that inside the plasma.

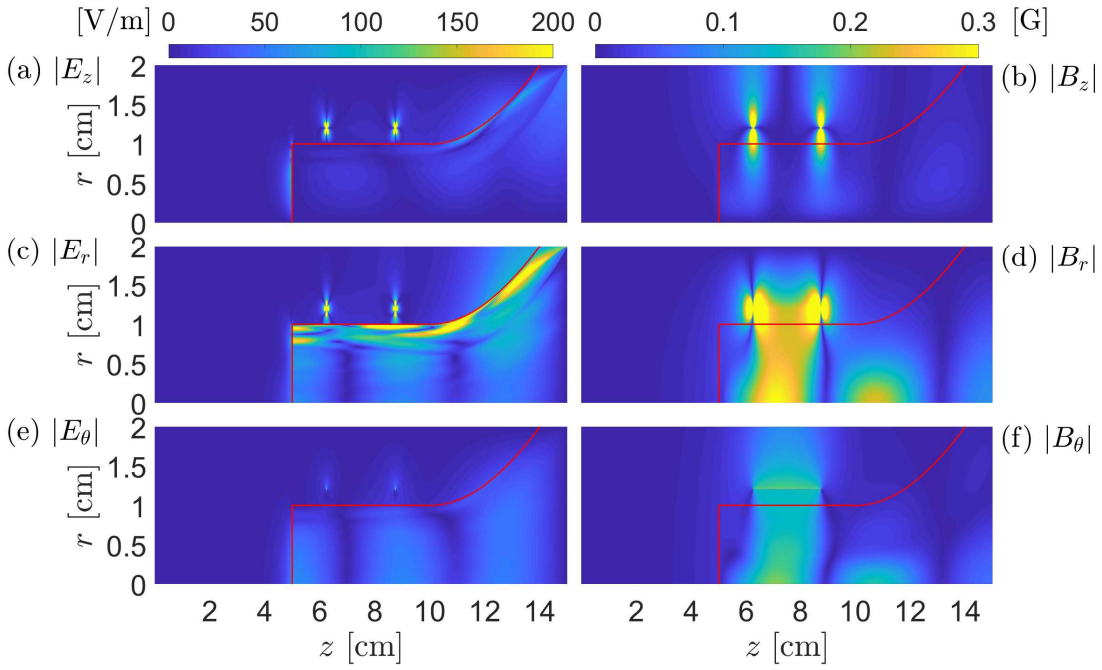

FIG. 5. Wavefield components in the nominal case and $m = 1$. All other parameters correspond to Table I. The red line delimits the extent of the plasma domain.

Finally, the vacuum chamber size affects the standing wave structure in the cavity. Notwithstanding this, it must be noted that since the wavelength in vacuum is large (about 22 m for the chosen excitation frequency), relatively large changes in vacuum size length or radius are needed to observe important modifications in the wavefields. The effect of the vacuum chamber size has been studied and discussed in Ref. 34 and 39.

IV. PARAMETRIC INVESTIGATION

This section explores the effect of varying the simulation parameters with respect to the nominal case of Table I. The magnitude of the applied magnetic field, plasma density, the effective collision frequency, and presence or absence of the plasma plume are investigated.

A. Applied magnetic field strength

The strength of the applied magnetic field $\boldsymbol{B}_a$ affects the electromagnetic wave propagation regime in the plasma through the dimensionless electron gyrofrequency, ω_{ce}/ω (and, relevant only in the high frequency domain, also the dimensionless lower-hybrid frequency ω_{lh}/ω), while its direction defines the local principal directions of the dielectric tensor $\bar{\bar{\kappa}}(z,r)$. The influence of the applied magnetic field strength in cylindrical homogeneous plasmas has been studied in the past[39,40]. Figure 6 shows the magnitude of E_r, B_r and the power absorption density w_p for two values of $B_a^\star$ that differ from the nominal simulation of Section III.

A larger magnetic field increases the E_r amplitude in the peripheral region, where the short-wavelength modes dominate. It also increases the axial wavelength of the helicon mode in the center of the plasma, and results in less numerous but wider power absorption peaks. This behavior is explained by the dispersion relation of the dominant parallel wavenumber eigenmode of the vacuum chamber cavity, for which $k_\parallel^2$ is inversely proportional to the ratio[37,38] ω_{ce}/ω. Among the simulated cases, $B_a^\star = 150$ G provides the maximum power deposition.

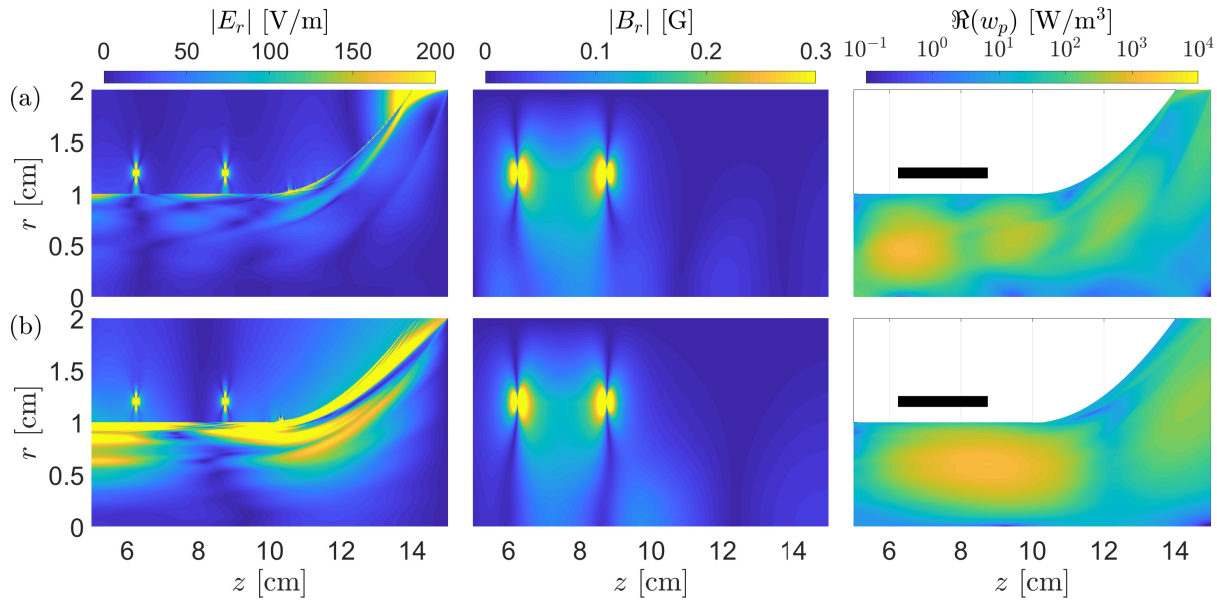

FIG. 6. 2D distribution of electromagnetic field and power density for two magnetic field strengths: $B_a^\star = 75$G (a; first row) and 300G (b; second row). All other parameters correspond to Table I.

Table II compares the $m = 1$ resistance R felt at the antenna for the different applied magnetic field strengths, and gives the fraction of absorbed power in the source and in the plasma plume regions. It is apparent that an optimal value of the magnetic field exists for which the total power absorption is maximal. A higher plasma resistance is typically desirable from the RF circuit design viewpoint.

The contributions of the source and plume regions to power absorption are comparable in all cases: although the power density in the plasma plume region is somewhat higher than in the source, this is compensated by the larger plasma volume there. This result, which is also visible in Fig. 6, suggests that the wave propagation and power deposition in the near region of the plasma plume cannot be neglected. This observation can have implications in the power balance (and thus in the efficiency) of HPT devices, where it is desirable to absorb all wave power within the source. This is necessary to maximize its efficiency, so that all absorbed power is available in the plasma from the beginning of the expansion into vacuum.

$B_a^\star$ [G]	Plasma resistance R		
	Total [mΩ]	Source	Plume
75	13.2	41%	59%
150	45	36%	64%
300	29.2	49%	51%
600	2.2	50%	50%

TABLE II. Comparison of plasma resistance and percentage of absorbed power in the helicon source and in the plasma plume for different values of $B_a^\star$ and $m = 1$. All other parameters are shown in Table I.

B. Plasma density

The wavefield and power absorption density profiles in Fig. 7 correspond to two different values of $n^\star$ with respect to the nominal case. The plasma density affects the dielectric tensor only through the dimensionless plasma frequency ω_{pe}/ω.

A larger $n^\star$ is seen to increase the amplitude of the wave field in the plasma domain, specially in the peripheral region, while preserving the axial structure of the standing wave. In

other words, the spacing between the peaks observed in the wave field and in the absorption density are not affected by the variation of magnitude of the plasma density[38].

The absorbed power also increases with $n^\star$ in the parametric range under consideration, as can be inferred from the figures and as summarized in Table III. Larger values of $n^\star$ bring about a stronger short-wavelength structure to the power absorption density, which is not present at lower densities, indicating a larger role of TG waves in power deposition.

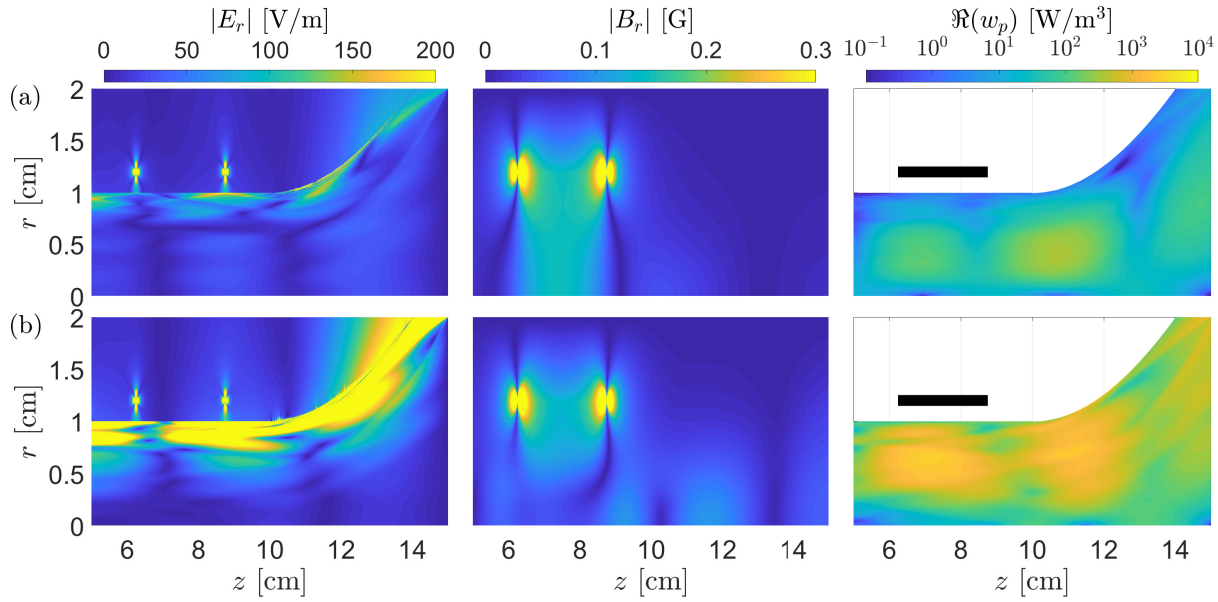

FIG. 7. 2D distribution of electromagnetic field and power density for different plasma density: a and b are $n^\star = 0.95 \times 10^{18}\ m^{-3}$ and $1.52 \times 10^{19}\ m^{-3}$, respectively. All other parameters correspond to Table I.

$n^\star$ [m^{-3}]	Plasma resistance R		
	Total [mΩ]	Plume	Total
0.95×10^{18}	4.2	41%	59%
3.8×10^{18}	45	36%	64%
1.52×10^{19}	55.5	41%	59%

TABLE III. Comparison of plasma resistance and percentage of absorbed power in the helicon source and in the plasma plume for different values of $n^\star$ and $m = 1$. All other parameters are shown in Table I.

C. Plasma collisionality

Electron collisionality is expected to be the dominant damping mechanism in the non-resonant interaction between the wave and a dense plasma compared to others such as Landau damping[25], and it is the only one included in the present model. Collisions only affect the dielectric tensor through the dimensionless factor $\nu_e^\star/\omega$.

The variation of resistance and reactance at the antenna as a function of $\nu_e^\star/\omega$ is shown in Fig. 8 for three values of the applied magnetic field strength at the reference $B_a^\star$. The effective collision frequency mainly affects the resistance R, while its influence on the reactance X is small. A nearly-constant impedance is desirable for the simplicity of the impedance matching part of the RF circuit that powers the device.

For each applied magnetic field strength, an optimal value of the $\nu_e^\star/\omega$ exists for which absorption is maximal, and this value increases with $B_a^\star$. The existence of an optimum collisionality can be explained as follows: while a very small collision frequency results in the plasma being an inefficient power absorber, a value too large can cause the reflection of the wave at the plasma surface and hinders the propagation of the RF power into the plasma, also reducing the deposited power. An intermediate value of $\nu_e^\star$ then results in a maximum power absorption and plasma resistance. This optimum is found at relatively small values of $\nu_e^\star/\omega$ for the nominal magnetic strength case.

The 2D power absorption density for different effective collision frequencies is shown in Fig. 9. It is evident that a small wavelength structure is present in the low collisionality cases, which is efficiently damped at higher values of $\nu_e^\star/\omega$. These small-wavelength structures become more relevant and intricate the lower $\nu_e^\star/\omega$, and required a finer numerical grid to resolve correctly. The spatial extent of the power absorption peaks and the propagation of the wave into the plume region diminish with increasing $\nu_e^\star/\omega$. This leads to less power deposition in downstream, as reflected by the integral results gathered in Table IV.

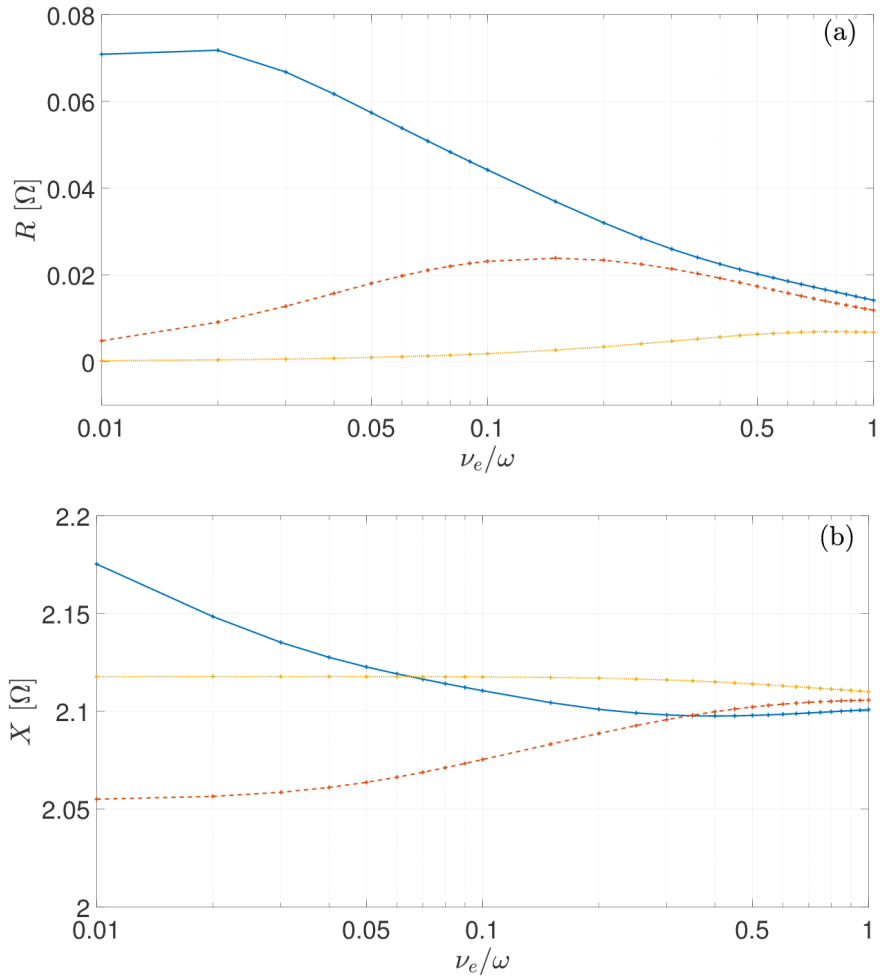

FIG. 8. Resistance and reactance at the antenna for $m = 1$ as a function of the effective electron collision frequency for $B_a^\star = 150$ (cross, blue), 300 (diamond, red), 600 (circle, black). All other parameters correspond to Table I.

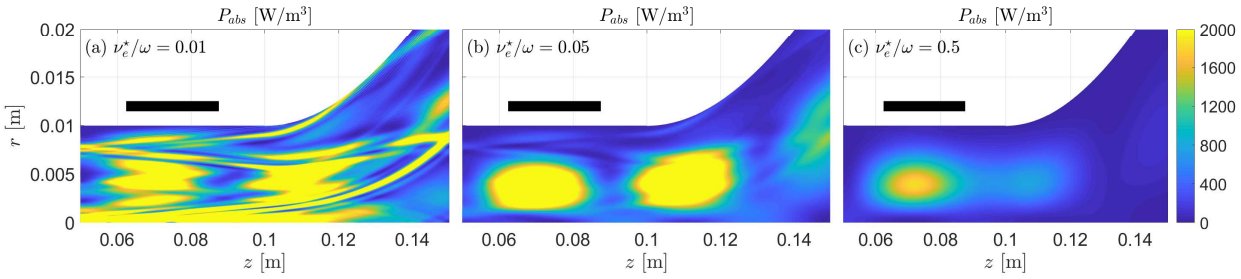

FIG. 9. Power absorption density $\Re(w_p)$ for different values of the effective electron collision frequency $\nu_e^\star$ and $m = 1$. All other parameters correspond to Table I.

$\nu_e^\star/\omega$	Plasma resistance R		
	Total [mΩ]	Source	Plume
0.01	70.9	36%	64%
0.05	57.4	38%	62%
0.1	45	36%	64%
0.5	20.2	67%	33%

TABLE IV. Comparison of plasma resistance and percentage of absorbed power in the helicon source and in the plasma plume for different values of $\nu_e^\star$ and $m = 1$. All other parameters are shown in Table I.

Finally, it is necessary to note that our choice of collision model (a constant ν_e in the plasma domain), while allowing us to simplify the analysis and separate the influence of the plasma density and the collisionality, differs from the expected collisionality profile in actual devices, where electron density (and temperature) gradients lead to a changing ν_e with position. Additionally, we have explored a rather wide range of $\nu_e^\star$, with values up to $\nu_e^\star = \omega$, well beyond those expected in actual HPTs. As the effective collisionality for power deposition in an actual device is not easily modeled (anomalous collision, for instance, may play an important role in the plasma source and the near plume region), it is hard to infer how a more realistic collisionality model would affect the present results.

D. Divergence of the plasma plume

The results obtained so far suggest that wave propagation into the diverging plasma plume region can be explained as a small modification of the classical cylindrical helicon wave theory. To complete the analysis and allow for direct comparison with existing purely-cylindrical results, two additional simulations are presented that replace the plasma plume region with an equivalent length of cylindrical plasma.

The wavefield and power absorption density for the source-only simulations with $B_a^\star = 150$ G and 300 G are shown in Fig. 10, and the comparison of the power absorption with the simulations that include a plasma plume is shown in Table V. The plots illustrate the standing wave structure in the plasma column. Again, the magnetic field strength governs the axial wavelength of this standing mode. Comparing with the plume case in Fig. 4-6, the

similar distributions of wave fields and power absorption conclude that the cylindrical helicon wave theory is still satisfied in the presence of the plasma plume, albeit the divergence of the plasma density and magnetic field lines causes a similar radial opening of the wavefield, with the waves being partially guided by the magnetic field.

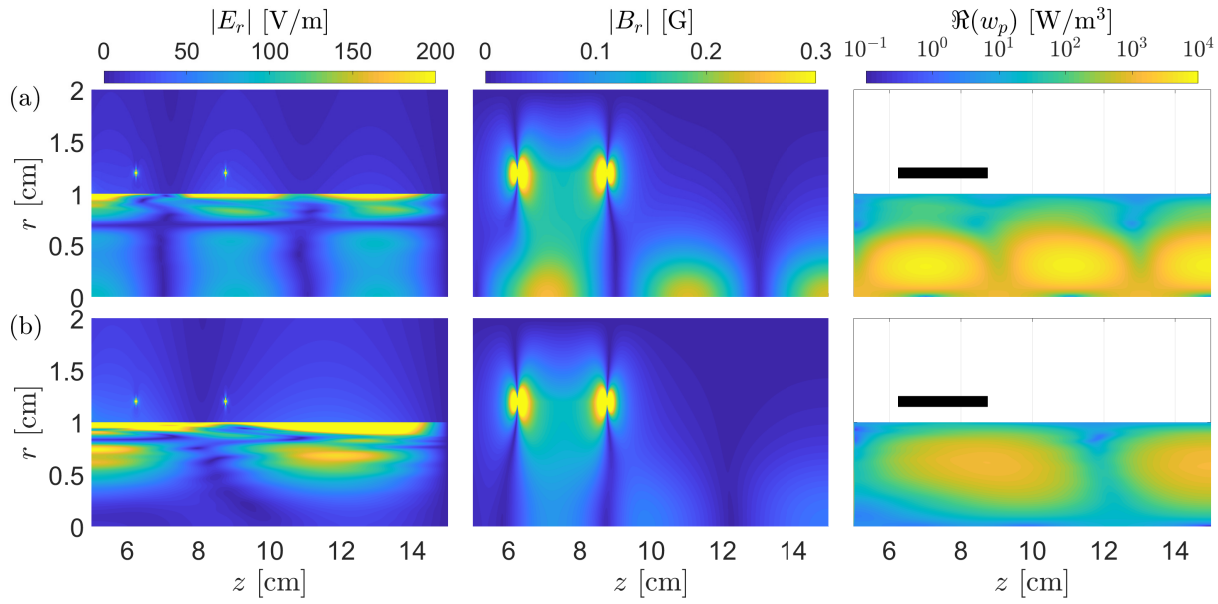

FIG. 10. 2D distribution of electromagnetic fields and power density for different magnetic fields in the source case for $m = 1$: $B_a^\star = 150$ G (a) and 300 G (b). All other parameters are shown in Table I.

Magnetic field $B_a^\star$	No plume [mΩ]		Plume [mΩ]	
	R	X	R	X
150 G	52	2120	45	2110
300 G	19.7	2094	29.2	2075
600 G	1.9	2130	2.2	2117

TABLE V. Comparison of resistance and reactance at the antenna between the no-plume and plume cases for two magnetic field strengths, for $m = 1$. All other parameters are shown in Table I.

V. CONCLUSIONS

A 2D time-harmonic plasma-wave model, based on a cold collisional plasma dielectric tensor, and integrated with the finite difference Yee's scheme with interpolation, has been used to study the propagation and absorption of electromagnetic power in the plasma region of a helicon plasma thruster contained in a laboratory vacuum chamber, taking into account the divergent magnetic field and plasma beam in the nozzle region.

It has been seen that the $m = 1$ azimuthal mode dominates over all others in the magnitude of the electromagnetic fields in the plasma and the absorbed power, to the point that all other azimuthal modes represent a negligible contribution. This is in agreement with existing studies of purely cylindrical plasmas. Based on this result, antennas that excite dominantly this mode in the plasma ought to be preferable. The thin Nagoya III used in this study excites all odd m modes equally in j_{za}, and with a $1/m$ law in $j_{\theta a}$. The model allows determining the spatial distribution of absorbed power density and the antenna impedance seen by the antenna in general plasma and magnetic field configurations, and can be matched to other partial models of the HPT, such as the DC plasma transport and the external RF electric circuit.

The influence of the applied magnetic field strength, the plasma density, and the effective electron collision frequency on the wavefield, power absorption, and antenna impedance has been investigated. Some of these parameters show an optimum in power absorption (i.e. plasma resistance) in the ranges under study. The resistance at the antenna is sensitive to the operating regime, whereas the reactance is shown to be essentially constant.

With respect to the known solution in a purely-cylindrical plasma column, the presence of a plasma plume downstream is seen to affect the wave field only partially. Wave propagation is guided by the curved geometry of the magnetic field, as it is apparent from the location along the magnetic lines of the peaks of power absorption. Importantly, power absorption is seen to occur not only in the cylindrical source region under the antenna, but also in the plume region. Indeed, in the present simulations, source and nozzle regions are responsible for roughly half of the power absorption. Therefore, we conclude that the plasma and magnetic field expansion that takes place in the plume region does not prevent the propagation of the wave into the near downstream region. This is not desirable for propulsive applications, where ideally all power should be deposited in the source and be available for

the acceleration of the plasma jet from the start.

Future work must assess other collisionality models and power absorption mechanisms, and more importantly integrate the wave-plasma model with the plasma transport model to produce full HPT simulations and with the RF electric circuit to estimate the overall efficiency of the system. This will allow a global understanding of the physics of HPT prototypes and the way to improve their efficiency up to competitive values. Only then, the study of the operation of the device in free space will make full sense. Certainly, it is expected that the absence of reflecting walls in free space will result in a non-standing wave structure and will diminish the total absorbed power by the plasma, both in the source region and in the plume region. Part of the power emitted by the antenna will be lost as free space space radiation, which could be mitigated by modifications on the thruster design. As the development of the HPT technology advances and approaches in-flight qualification, free-space simulations will become necessary. These will likely require the implementation of non-reflecting boundary conditions (e.g. perfectly-matched layers).

ACKNOWLEDGMENTS

The authors acknowledge the initial development of the present model by V. Gómez and J. Navarro. This work was supported by the Spain's National Research and Development Plan (Project ESP2016-75887). Bin Tian was supported by a PhD grant from the Chinese Scholarship Council.

Appendix A: Nagoya III antenna current

The antenna current density $\boldsymbol{j}_a(z,r)$ is the source term in Maxwell equations (2)- (7). The simulations in this paper use an ideal thin-plate Nagoya III antenna of mean radius r_a, with the thickness d_t, with $d_t \ll 2r_a$. Then, the radial component of current density j_{ra} is negligible, and[41]

$$j_{za} = \frac{I_a}{\pi r_a} G\,(r)\, H(z-z_1) H(z_2-z) \text{ if } m \text{ odd; } j_{za} = 0 \text{ otherwise,} \tag{A1}$$

$$j_{\theta a} = i \frac{r_a}{m} \frac{\partial j_{za}}{\partial z} \tag{A2}$$

where I_a is the current amplitude in the antenna, z_1 and $z_2 = z_1 + L_a$ are the positions of the axial ends of the antenna. In Eq. (A1), H represents the Heaviside step function, and $G(r)$ is a Gaussian function profile used to avoid a sharp current density radial gradient at the antenna border, which for $r \in [r_a - d_t/2, r_a + d_t/2]$ is equal to[19]:

$$G(r) = \frac{2a}{\sqrt{\pi} d_t} \exp\left(-4a^2 \frac{(r - r_a)^2}{d_t^2}\right), \tag{A3}$$

where $a = d_t/2\sqrt{2}\Delta r$ has been chosen. In eq. (A2), $j_{\theta a}$ is computed from j_{za} by imposing that the antenna current is divergence free[19,23], $\nabla \cdot \boldsymbol{j}_a = 0$, a characteristic of loop-like antennas in the low frequency regime[17,19]. From the functional dependency of j_{za} and $j_{\theta a}$ in Eq. (A1) and (A2), it is evident that only odd azimuthal modes m are applicable for the Nagoya III antenna[41,42].

REFERENCES

[1]T. Ziemba, J. Carscadden, J. Slough, J. Prager, and R. Winglee. High power helicon thruster. In *41th AIAA/ASME/SAE/ASEE Joint Propulsion Conference & Exhibit*, AIAA 2005-4119, 2005.

[2]M. West, C. Charles, and R. Boswell. Testing a helicon double layer thruster immersed in a space-simulation chamber. *Journal of Propulsion and Power*, 24(1):134–141, 2008.

[3]O. Batishchev. Minihelicon plasma thruster. *IEEE Transaction on Plasma Science*, 37(8):1563–1571, 2009.

[4]D. Pavarin, F. Ferri, M. Manente, D. Curreli, D. Melazzi, D. Rondini, and A. Cardinali. Development of plasma codes for the design of mini-helicon thrusters. In *32th International Electric Propulsion Conference*, 2011.

[5]B. Longmier, E. Bering, M. Carter, L. Cassady, W. Chancery, F. Díaz, T. Glover, N. Hershkowitz, A. Ilin, G. McCaskill, et al. Ambipolar ion acceleration in an expanding magnetic nozzle. *Plasma Sources Science and Technology*, 20:015007, 2011.

[6]J. Navarro, M. Wijnen, P. Fajardo, M. Merino, and E. Ahedo. Experimental performances of a 1 kw hpt by means of plasma diagnostics. In *35th International Electric Propulsion Conference*, IEPC-2017-447, 2017.

[7]J. Navarro, M. Wijnen, P. Fajardo, and E. Ahedo. Experimental characterization of a 1 kw helicon plasma thruster. *Vacuum*, 149:69–73, 2018.

[8]E. Ahedo. Plasmas for space propulsion. *Plasma Physics and Controlled Fusion*, 53(12):124037, 2011.

[9]R. Boswell and F. Chen. Helicons-the early years. *Plasma Science, IEEE Transactions on*, 25(6):1229–1244, 1997.

[10]F. Chen and R. Boswell. Helicons-the past decade. *Plasma Science, IEEE Transactions on*, 25(6):1245–1257, 1997.

[11]E. Ahedo and M. Merino. Two-dimensional supersonic plasma acceleration in a magnetic nozzle. *Physics of Plasmas*, 17(7):073501, 2010.

[12]M. Merino and E. Ahedo. Magnetic nozzles for space plasma thrusters. In J. Leon Shohet, editor, *Encyclopedia of Plasma Technology*, volume 2, pages 1329–1351. Taylor and Francis, 2016.

[13]K. Takahashi, T. Lafleur, C. Charles, P. Alexander, R. Boswell, M. Perren, R. Laine, S. Pottinger, V. Lappas, T. Harle, et al. Direct thrust measurement of a permanent magnet helicon double layer thruster. *Applied Physics Letters*, 98(14):141503, 2011.

[14]C. Charles, R. Boswell, and K. Takahashi. Investigation of radiofrequency plasma sources for space travel. *Plasma Physics and Controlled Fusion*, 54(12):124021, 2012.

[15]K. Takahashi, A. Chiba, A. Komuro, and A. Ando. Axial momentum lost to a lateral wall of a helicon plasma source. *Physical Review Letters*, 114(19):195001, 2015.

[16]E. Ahedo and J. Navarro. Helicon thruster plasma modeling: Two-dimensional fluid-dynamics and propulsive performances. *Physics of Plasmas*, 20(4):043512, 2013.

[17]Y. Mouzouris and J. Scharer. Wave propagation and absorption simulations for helicon sources. *Physics of Plasmas*, 5(12):4253–4261, 1998.

[18]M. Carter, F. Baity Jr, G. Barber, R. Goulding, Y. Mori, D. Sparks, K. White, E. Jaeger, F. Chang-Diaz, and J. Squire. Comparing experiments with modeling for light ion helicon plasma sources. *Physics of Plasmas*, 9:5097, 2002.

[19]G. Chen, A. Arefiev, R. Bengtson, B. Breizman, C. Lee, and L. Raja. Resonant power absorption in helicon plasma sources. *Physics of plasmas*, 13:123507, 2006.

[20]R. Kinder and M. Kushner. Noncollisional heating and electron energy distributions in magnetically enhanced inductively coupled and helicon plasma sources. *Journal of Applied Physics*, 90:3699, 2001.

[21]K. Yee. Numerical solution of initial boundary value problems involving maxwell's equations in isotropic media. *IEEE Transactions on Antennas and Propagation*, 14(3):302–307,

1966.

[22]B. Tian, E. Ahedo, and M. Merino. Development and validation of a 2d wave-plasma code for helicon plasma thrusters. In *Space Propulsion Conference*, SPC 2016-3124913, Rome, Italy, 2016. European Space Agency.

[23]L. Chang, M. Hole, J. Caneses, G. Chen, B. Blackwell, and C. Corr. Wave modeling in a cylindrical non-uniform helicon discharge. *Physics of Plasmas*, 19(8):083511, 2012.

[24]F. Chen. Helicon discharges and sources: a review. *Plasma Sources Science and Technology*, 24(1):014001, 2015.

[25]F. Chen and D. Blackwell. Upper limit to landau damping in helicon discharges. *Physical Review Letters*, 82(13):2677–2680, 1999.

[26]F. Chen. Plasma ionization by helicon waves. *Plasma Physics and Controlled Fusion*, 33(4):339, 1991.

[27]T. Stix. *Waves in plasmas*. Springer, 1992.

[28]J. Young. A full finite difference time domain implementation for radio wave propagation in a plasma. *Radio Science*, 29(6):1513–1522, 1994.

[29]S. Cummer. An analysis of new and existing fdtd methods for isotropic cold plasma and a method for improving their accuracy. *IEEE Transactions on Antennas and Propagation*, 45(3):392–400, 1997.

[30]M. Merino, A. Sanchez-Villar, E. Ahedo, P. Bonoli, J. Lee, A. Ram, and J. Wright. Wave propagation and absorption in ECR plasma thrusters. In *35th International Electric Propulsion Conference*, IEPC-2017-105, Fairview Park, OH, 2017.

[31]B. Tian. *Modeling of Physical Processes in Radio-frequency Plasma Thrusters*. PhD thesis, Universidad Carlos III de Madrid, 2017.

[32]M. Light and F. Chen. Helicon wave excitation with helical antennas. *Physics of Plasmas*, 2(4):1084–1093, 1995.

[33]I. Sudit and F. Chen. Discharge equilibrium of a helicon plasma. *Plasma Sources Science and Technology*, 5(1):43, 1996.

[34]I. Kamenski and G. Borg. An evaluation of different antenna designs for helicon wave excitation in a cylindrical plasma source. *Physics of Plasmas*, 3(12):4396–4409, 1996.

[35]D. Arnush and F. Chen. Generalized theory of helicon waves. ii. excitation and absorption. *Physics of Plasmas*, 5(5):1239–1254, 1998.

[36]M. Krämer. Propagation and damping of m=+ 1 and m=- 1 helicon modes in an inhomogeneous plasma column. *Physics of Plasmas*, 6(4):1052–1058, 1999.

[37]C. Lee, G. Chen, A. Arefiev, R. Bengtson, and B. Breizman. Measurements and modeling of radio frequency field structures in a helicon plasma. *Physics of Plasmas*, 18(1):013501, 2011.

[38]B. Breizman and A. Arefiev. Radially localized helicon modes in nonuniform plasma. *Physical Review Letters*, 84(17):3863, 2000.

[39]B. Tian, E. Ahedo, and J. Navarro-Cavalle. Investigation of plasma-wave interaction in helicon antenna thrusters. In *50th AIAA/ASME/SAE/ASEE Joint Propulsion Conference & Exhibit*, AIAA 2014-3475, 2014.

[40]K. Shamrai, V. Pavlenko, and V. Taranov. Excitation, conversion and damping of waves in a helicon plasma source driven by an m= 0 antenna. *Plasma Physics and Controlled Fusion*, 39(3):505, 1997.

[41]S. Cho. The field and power absorption profiles in helicon plasma resonators. *Physics of Plasmas*, 3(11):4268–4275, 1996.

[42]K. Shamrai and V. Taranov. Resonance wave discharge and collisional energy absorption in helicon plasma source. *Plasma Physics and Controlled Fusion*, 36(11):1719, 1994.